photonics

MDPI

Article

Synergy of Nd:YAG Picosecond Pulsed Laser Irradiation and Electrochemical Anodization in the Formation of TiO_2 Nanostructures for the Photocatalytic Degradation of Pesticide Carbofuran

Miloš Tošić [1], Vladimir Rajić [1], Dejan Pjević [1], Stevan Stojadinović [2], Nikša Krstulović [3], Suzana Dimitrijević-Branković [4] and Miloš Momčilović [1,*]

[1] Vinča Institute of Nuclear Sciences—National Institute of the Republic of Serbia, University of Belgrade, Mike Petrovića Alasa 12-14, 11351 Belgrade, Serbia; milos.tosic@vin.bg.ac.rs (M.T.); vladimir.rajic@vin.bg.ac.rs (V.R.); dejanp@vin.bg.ac.rs (D.P.)
[2] Faculty of Physics, University of Belgrade, Studentski trg 12-16, 11000 Belgrade, Serbia; sstevan@ff.bg.ac.rs
[3] Institute of Physics, Bijenička Cesta 46, 10000 Zagreb, Croatia; niksak@ifs.hr
[4] Faculty of Technology and Metallurgy, University of Belgrade, Karnegijeva 4, 11000 Belgrade, Serbia; suzana@tmf.bg.ac.rs
* Correspondence: milos@vin.bg.ac.rs

Abstract: This study proposes a simple and controlled method for producing TiO_2 with phase junction, oxygen vacancies, and Ti^{3+} by combining picosecond pulsed laser irradiation and electrochemical anodization. Ti mesh was pretreated by irradiating with a picosecond pulsed laser technique using an Nd:YAG laser (1064 nm) at two fluencies, 15 J/cm^2 and 30 J/cm^2. The samples were then subjected to electrochemical anodization to form TiO_2 nanotube arrays on the previously laser-treated surface. This study will investigate the possibility of forming TiO_2 nanotube arrays on a pre-laser-treated Ti substrate and determine their physicochemical and photocatalytic properties. The samples were characterized by FESEM, XRD, Raman, XPS, and UV-Vis DRS. UV-Vis spectroscopy was used to observe the progress of photocatalytic degradation for all samples, and degradation products were determined using GC-MS. With the synergistic effects of phase junction, oxygen vacancies, and Ti^{3+}, the laser-treated TiO_2 with 30 J/cm^2 showed a higher photocatalytic degradation rate (85.1%) of the pesticide carbofuran compared to non-laser-treated TiO_2 (54.8%), remaining stable during successive degradation cycles, which has promising practical applications.

Keywords: Nd:YAG picosecond pulsed laser; electrochemical anodization; TiO_2; photocatalytic degradation; carbofuran

Citation: Tošić, M.; Rajić, V.; Pjević, D.; Stojadinović, S.; Krstulović, N.; Dimitrijević-Branković, S.; Momčilović, M. Synergy of Nd:YAG Picosecond Pulsed Laser Irradiation and Electrochemical Anodization in the Formation of TiO_2 Nanostructures for the Photocatalytic Degradation of Pesticide Carbofuran. *Photonics* **2024**, *11*, 284. https://doi.org/10.3390/photonics11030284

Received: 23 February 2024
Revised: 12 March 2024
Accepted: 20 March 2024
Published: 21 March 2024

1. Introduction

In recent years, significant efforts have been dedicated to developing new photoactive materials for solar-driven water purification. Titanium dioxide (TiO_2), due to its high efficiency, non-toxicity, and excellent stability, is widely used as a photocatalyst to produce reactive oxygen species (ROS) such as highly reactive hydroxyl radicals ($^{\bullet}OH$) and superoxide radical anions ($^{\bullet}O_2^-$) in photocatalysis [1–4]. Due to these properties, it is used to degrade organic pollutants into harmless forms, ideally into the final products CO_2 and H_2O [5]. Photocatalysis is a process where electron-hole pairs are created with excitation energy ($h\nu$) that is greater than or equal to the band gap energy of the catalyst. As a result, electrons move from the valence band to the conduction band, leading to the separation of photogenerated charge carriers. This separation facilitates the catalysis process [6,7]. The photocatalytic properties of TiO_2 are widely recognized, but it has some limitations due to its large band gap (3.2 eV) [8]. This means that it can only absorb light in the UV region (which represents only 5% of the solar spectrum), limiting its usefulness in harnessing solar

energy. Additionally, the photogenerated electron/hole tends to recombine quickly, which reduces the quantum efficiency [9].

TiO_2 nanotube/nanoporous structures are very interesting for photocatalytic applications due to their large surface area, high physical stability, good adsorption ability, superior electron transport rates, and excellent photoelectrochemical properties. In comparison, spherical nanopowders are very limited in their utilization of radiation compared to the tubular structure, where light trapping leads to a larger surface area of irradiated TiO_2 and thus results in higher photocatalytic efficiency [10].

The two most common phases of TiO_2 are anatase and rutile, with different properties and thermodynamic stability [11]. The anatase phase of TiO_2 is preferred for use in photocatalytic processes, such as hydrogen generation in water and photodegradation of organic molecules in water and air. On the other hand, TiO_2 in the rutile phase is preferred for use in optoelectronic devices such as UV photodetectors and UV light sources. Anatase has a larger band gap than rutile, while rutile is thermodynamically more stable than anatase [12,13].

The TiO_2 recombination of photo-induced charge carriers can be reduced by introducing atomic-scale defects such as Ti^{3+} and oxygen vacancies (V_O), and thus enhance its photocatalytic performance [14,15]. V_O affects the recombination rate of electron/hole (e^-/h^+) pairs in photocatalysis, altering charge transfer and surface adsorption. Ti^{3+} and V_O defects impact reactivity and generate ROS, activating molecules of contaminants [16–18]. Different strategies, including hydrogenation, thermal reduction, electrochemical reduction, and liquid-phase reduction, have been developed to introduce V_O in TiO_2 lattices. However, certain strategies may require high temperatures, harsh synthetic conditions, or toxic chemicals, which can be challenging [19,20].

Ultrashort laser pulses (picosecond or femtosecond), as an environmentally friendly method, can be used to treat and improve the surface properties of metals [21–23]. Laser irradiation fluence tunes the kinetic energy of species in the plasma plume, influencing surface mobility that impacts nucleation events and deposit growth. Applying a precise amount of laser energy to a restricted area can result in a desired physical modification or chemical reaction, which can be carefully controlled by laser parameters [21,24,25]. When exposed to laser irradiation, a titanium surface rapidly heats up, forming a high-temperature plasma that causes instantaneous chemical reactions. These reactions lead to changes in the composition of the processed area, forming V_O by deforming and fracturing the chemical bonds of TiO_2 [26]. Furthermore, the presence of reactive oxygen atoms initiates chemical reactions and modifies laser-treated titanium, leading to the formation of TiO_2 structures [27]. The anatase phase of TiO_2 transforms to a rutile phase under a high dose of laser irradiation due to rutile stability at high temperatures and pressures induced by pulsed laser irradiation [22]. The significant boost in photocatalytic activity directly results from the synergistic effects between the two phases present in the mixture [28,29]. Furthermore, the charge transfer from anatase to rutile at their interfaces unequivocally amplifies their effectiveness. Due to the band alignment, a potential gradient is created at the anatase/rutile heterojunction by the opposing buildup of e^- and h^+, which can prevent their recombination [30]. It can be concluded that by using pulsed laser technology and controlling laser parameters, it is possible to create a TiO_2 layer on a Ti substrate with a mixture of phases during the transformation process from anatase to rutile phase [25].

J. Wawrzyniak et al. [31] have shown the effects of laser treatment at different angles on TiO_2 nanotube arrays, changing their morphology and promoting the creation of favorable localized states within the band gap of the material. Białous et al. [21] reported that the mixed phases of nanoporous TiO_2 films produced by pulsed laser in air at atmospheric pressure have an anatase content of over 70%. However, the resulting phase of the TiO_2 layer can vary depending on the intensity and dose of irradiation. Arthurs Medvids et al. [22] concluded that the TiO_2 layer on Ti grows with increasing laser dose, but the photocatalytic decomposition reaction constantly decreases. This behavior can be explained by phase mixing in the TiO_2 layer. At higher laser doses, the TiO_2 layer partially transforms into

the rutile phase, and a deficit of O atoms occurs deeper in the Ti substrate due to the low diffusion of O atoms in Ti.

Photocatalysis has been proposed as an effective technique for treating aqueous carbofuran (CBF) in the presence of TiO_2 as a photocatalyst [32–34]. Carbofuran (2,3-dihydro-2,2-dimethyl-7-benzofuranyl methylcarbamate) is a carbamate pesticide that is widely used as an insecticide and nematicide on a variety of agricultural crops. It is highly toxic to humans when ingested or inhaled and may pose a significant risk to those in direct contact, such as those working in manufacturing or crop fields. It is recognized as fairly persistent in soil and aquatic ecosystems in neutral or acidic conditions and is extremely toxic to mammals, birds, fish, and wildlife [35].

In this work, TiO_2 nanotube arrays were synthesized on previously picosecond pulsed laser-treated Ti mesh using the 1064 nm wavelength of Nd:YAG lasers at two different fluencies. This study compared the effectiveness of non-laser-treated TiO_2 and laser-treated TiO_2 samples for degrading CBF. Their photodegradation efficiency was tested under simulated sunlight irradiation to determine the photocatalytic enhancement. This study also identified the products of CBF generated during the photocatalytic degradation process and proposed a degradation pathway based on the formation of intermediates. To the best of our knowledge, this study is the first to investigate the photocatalytic properties of TiO_2 nanotube arrays grown on a pretreated Ti substrate using a picosecond pulsed laser and to examine the photocatalytic degradation of CBF using TiO_2 nanotube arrays.

2. Materials and Methods

2.1. Reagents and Chemicals

Carbofuran 99.65 wt% ($C_{12}H_{15}NO_3$, 221.25 g/mol) was purchased from Dr. Ehrenstorfer, LGC Standards Ltd. (Augsburg, Germany), titanium mesh (Ti) from Goodfellow, Wrexham, UK, ethylene glycol 99.5 wt% ($C_2H_6O_2$, 62.07 g/mol) form Centrohem (Stara Pazova, Serbia), nitric acid 65 wt% (HNO_3, 63.01 g/mol), and acetic acid 99.5 wt% (CH_3COOH 60.05 g/mol) from Zorka Pharma (Šabac, Serbia). Hydrofluoric acid 50 wt% (HF, 20.01 g/mol) from Alkaloid Skopje (Skopje, North Macedonia), sulfuric acid 98 wt% (H_2SO_4, 98.08 g/mol) from AnalaR Normapur (VWR Chemicals, Oslo, Norway) and ammonium fluoride—pro analysis 95 wt% (NH_4F, 37.04 g/mol) was obtained from Merck (Rahway, NJ, USA).

2.2. Synthesis of Photocatalysts

2.2.1. Pulsed Laser-Induced Oxidation Method

The Ti meshes underwent cleaning through sonication in acetone, ethanol, and distilled water, each for 10 min. Electrochemical and chemical polishing were performed on the samples [1]. The electrochemical polishing was carried out in a mixture of acetic acid (99.5 wt%), sulfuric acid (98 wt%), and hydrofluoric acid (50 wt%) (60:15:25 in volume) at an applied current of 0.7 A/cm^2. The final chemical polishing was conducted in a mixture of HF (50 wt%) and nitric acid (65 wt%) (1:3 in volume), followed by immersion in water. The synthesis of TiO_2 was performed by irradiating a titanium mesh with a pulsed laser in air at atmospheric pressure and room temperature. Irradiation was performed with a picosecond Nd:YAG laser (Ekspla SL 212/SH/FH, 150 ps) operating at a wavelength of 1064 nm and a repetition rate of 10 Hz at two fluencies, 15 J/cm^2 and 30 J/cm^2. During the irradiation, the laser was focused on the Ti target using a 15.2 cm lens. The spot size is 0.1 mm^2. The Ti mesh was precisely ablated using a motorized *XY* translation stage. The surface of the Ti mesh was scanned until an irradiated surface of 1 × 1 cm was achieved. The Ti mesh was irradiated on both sides under the same conditions. The samples were named L15TiO_2 and L30TiO_2 for 15 J/cm^2 and 30 J/cm^2, respectively.

2.2.2. Electrochemical Anodization and Annealing

TiO_2 nanotube arrays were produced on non-treated and laser-treated Ti meshes through a two-step process of electrochemical anodization [1] in a two-electrode electro-

chemical cell. The cell was connected to a power supply (Peak Tech® 6227, Chippenham, UK), with Ti mesh (1 × 2 cm) as the working electrode and platinum mesh as the counter electrode, placed 1.5 cm apart. The first step of electrochemical anodization was conducted at room temperature with magnetic stirring in an ethylene glycol solution consisting of 0.3 wt% NH_4F and 2% H_2O at 50 V for 40 min. After the first step, the TiO_2 nanotube arrays were formed, which were then removed by sonication using an ultrasonic water bath. The second step of anodization was conducted with a fresh and identical electrolyte ratio at 50 V for 15 min. After the second anodization, TiO_2 nanotube arrays were again formed, and the samples were then washed with water and dried. Finally, the TiO_2, $L15TiO_2$, and $L30TiO_2$ photocatalyst samples were placed in a ceramic crucible and annealed in air at 450 °C for 1 h, at a rate of 5 °C/min [36]. The purpose of the annealing treatment was to unify the structure of the investigated materials. The experimental setup is shown in Figure 1.

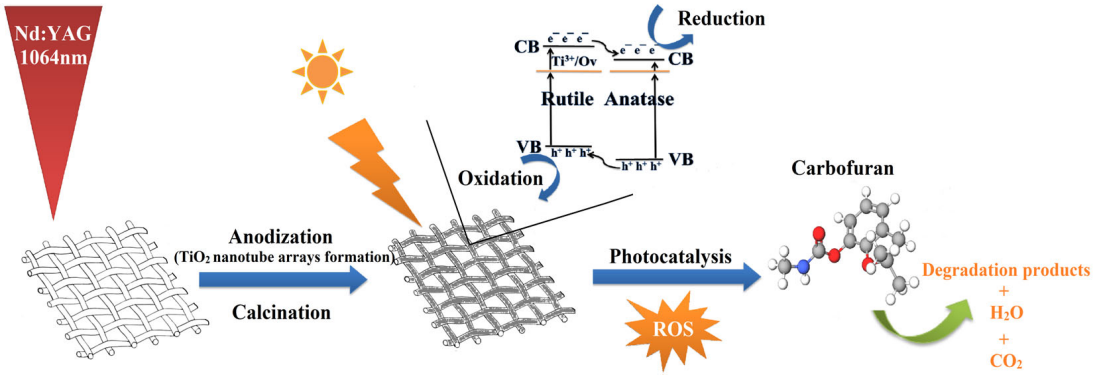

Figure 1. Schematic of the experimental setup.

2.3. Characterization

To determine the morphology of the TiO_2, $L15TiO_2$, and $L30TiO_2$ that were synthesized, a field emission scanning electron microscope (FESEM) on Scios 2 DualBeam (Thermo Fisher Scientific, Waltham, MA, USA) was used. The crystal structures of the photocatalyst samples were detected by X-ray diffraction (XRD) using Rigaku Ultima IV (Rigaku, Tokyo, Japan) with CuKα radiation (λ = 1.54178 Å, 40 kV, 40 mA) in the 2θ range from 20° to 80° diffraction angle at a scanning rate of 2° min^{-1} and with a step of 0.05°. A Raman spectrometer system (Horiba Jobin Yvon, Paris, France) equipped with the Olympus BX 41 microscope (Olympus, Tokyo, Japan) was used in this study. Samples were recorded using a laser at a wavelength of 532 nm equipped with a 600 lines/mm grating, using ×50 objective, 10 s acquisition time, and utilizing 100% of laser power in the range of 100–1000 cm^{-1}. Chemical analysis was carried out by X-ray photoelectron spectroscopy (XPS), using SPECS Systems with XP50M X-ray source (SPECS Surface Nano Analysis GmbH, Berlin, Germany) for Focus 500 and PHOIBOS 100/150 analyzer with Al Kα source (1486.74 eV) at a 12.5 kV and 32 mA. To study the light absorption performance, the optical properties of the samples were measured on Shimadzu UV-2600i (DR UV-Vis, Shimadzu, Kyoto, Japan) using $BaSO_4$ as a reference.

2.4. Testing of the Photocatalytic Properties and Analysis of Photodegradation Products

In order to evaluate the photocatalytic properties of the synthesized samples, a 20 mL solution of CBF with a concentration of 4 mg/L was degraded under simulated sunlight irradiation using an Osram Ultra-vitalux 300 W (Osram, Munich, Germany) lamp. The lamp's light intensity was measured to be 300 W/m^2 using a Voltcraft PL-110SM Solar Measuring Instrument (Voltcraft, Wollerau, Germany). The specified spectral distribution for the lamp is shown in Figure S1. Samples with a modifying/working area of 1 × 1 cm were placed in the solution, and stirring was maintained throughout the photocatalytic degradation process. To maintain the room temperature, the reactor with a double-walled

cooling-water jacket was used throughout all experiments. The samples were then irradiated at a distance of 10 cm. To achieve adsorption–desorption equilibrium, the CBF solution was left in the dark for 30 min, after which it was irradiated for photocatalytic degradation. Every 1 h, 3 mL of the CBF solution was taken to determine the concentration using UV/Vis spectroscopy (LLG-uniSPEC 2). After each measurement, the extracted solution was returned to the reactor. The concentration of CBF can be detected by measuring any change in absorbance intensity, as it is directly proportional to the absorbance signal. The concentration of the CBF was assessed at the absorption maximum during photocatalysis for each sample at a specific wavelength. For the control test, the CBF solution was irradiated under the same conditions as the other samples but without the presence of TiO_2 samples. The control test did not show any change in absorbance and, therefore, in the concentration of CBF. The photocatalytic degradation efficiency of CBF is calculated by using Equation (1):

$$Degradation\ efficieny\ (\%) = \frac{C_0 - C}{C_0} \times 100 \quad (1)$$

where C_0 and C represent the initial concentration of CBF and the CBF concentration at the time t, respectively [37]. Photocatalytic degradation and degradation products were also confirmed using the GC-MS (Agilent GC 7890B/5977B mass detector, (Agilent, Santa Clara, CA, USA) technique.

3. Results and Discussion

3.1. Morphology

The TiO_2, L15TiO_2, and L30TiO_2 microstructures were observed by FESEM images. From the top and cross-section image (Figure 2a), the geometric parameters could be determined, including the length of the nanotube arrays, which was approximately 2.5 µm with an inner diameter of 130 nm for the TiO_2 sample. The nanotube layers have a clear periodic nanoring structure on the top and highly aligned vertical nanotube arrays underneath. Figure 2b shows the Ti mesh after pulsed laser irradiation and electrochemical anodization. Figure 2c displays the surface of the L15TiO_2 sample where visible laser traces are present due to ablation during movement on the *XY* translation stage.

Upon further investigation, two more types of nanotube arrays can be observed in L15TiO_2 (Figure 2d–f) and L30TiO_2 (Figure 2g–i) at and adjacent to the ablation center site. Underdeveloped nanotube arrays can be observed in the center of the ablation (Figure 2d,g). Moving away from the ablation center, disordered nanotube arrays can be observed, which were most probably created by the indirect effect of the pulsed laser, and in some areas, they merge at their tips, forming tubular nano-grass nanotubes (Figure 2e,h). Upon further observation, a transition between disordered and ordered nanotube arrays can be noticed (Figure 2f,i). It can be assumed that this appearance of different morphologies of nanotube arrays of laser-treated TiO_2 samples can be attributed to the Gaussian profile of the laser irradiation [38,39]. In this profile, the central part of the beam has the highest intensity, which later leads to the formation of one type of nanotube array. On the other hand, lower intensities outside the central part result in the formation of another type of nanotube array. We believe that the different morphologies result from applying different laser output energies, resulting in different temperatures on the Ti surface and varying Gaussian distributions. It can be concluded that laser ablation plays a key role in forming the morphology of L15TiO_2 and L30TiO_2 samples.

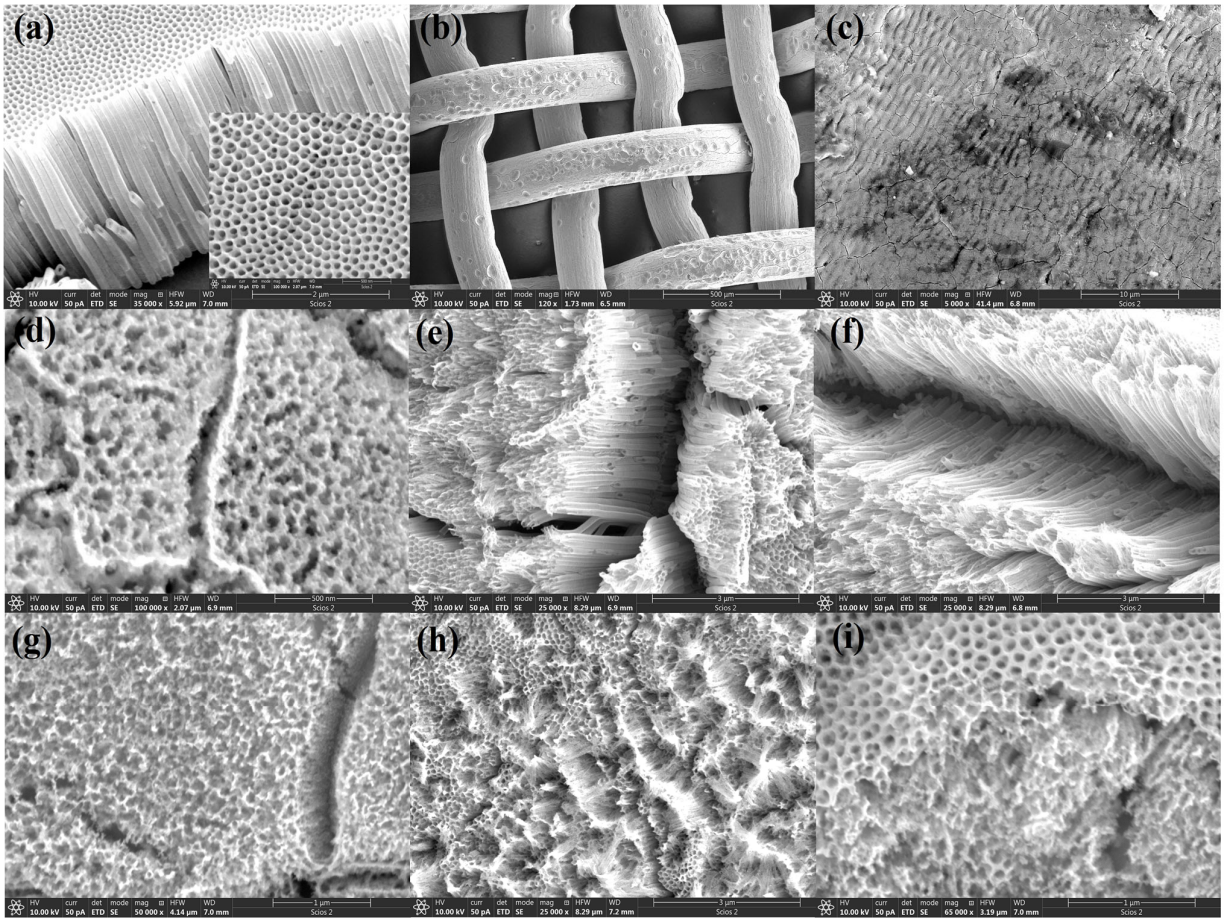

Figure 2. FESEM images of the (**a**) TiO_2 nanotube arrays structure, (**b**) laser irradiated and anodized Ti mesh, (**c**) surface of the L15TiO_2, (**d**–**f**) L15TiO_2 nanotube arrays structures, (**g**–**i**) L30TiO_2 nanotube arrays structures.

3.2. Structural Properties

X-ray diffraction (XRD) patterns of TiO_2, L15TiO_2, and L30TiO_2 are shown in Figure 3.

In all recorded samples, the strong reflections observed at 2θ equal to 35.1°, 38.4°, 40.2°, 53.0°, 63.0°, 70.6°, 76.2°, and 77.3° can be assigned to the (100), (002), (101), (102), (110), (103), (112), and (201) (JCPDS card No. 21-1294) crystal planes of the metallic Ti (T), respectively. The anatase phase (A) was also produced, which could be observed by its characteristic planes (101), (004), (200), (105), and (211) (JCPDS file No. 21-1272) at 25.3°, 37.7°, 48°, 53.8°, and 55°, respectively. Also, a small amount of rutile phase (R) can be observed at 27.6° (110) (JSPDS file No. 21-1276) in the L30TiO_2 sample.

The Raman spectra were collected from three different places in each sample, at the center and towards the vertical edges. As shown in Figure 4a, TiO_2 main peaks at 147, 400, 519, and 640 cm^{-1} can be assigned to anatase active modes $Eg_{(1)}$, $Bg_{(1)}$, $Ag_{(1)}$, and $Eg_{(3)}$, respectively [27]. The positions of the signals corresponding to the main mode of the active anatase $Eg_{(1)}$ of the laser-treated samples depend on the energy fluence used during the laser modifications, where $Eg_{(1)}$ is found at 151 cm^{-1} for 15 J/cm^2 and 153 cm^{-1} for fluence energy of 30 J/cm^2 (inset Figure 4b). This blue shift is typically attributed to the presence of V_O that results from the degradation of the crystal structure in the defective TiO_2 [31,40]. Raman data for all samples were previously normalized for easier comparison.

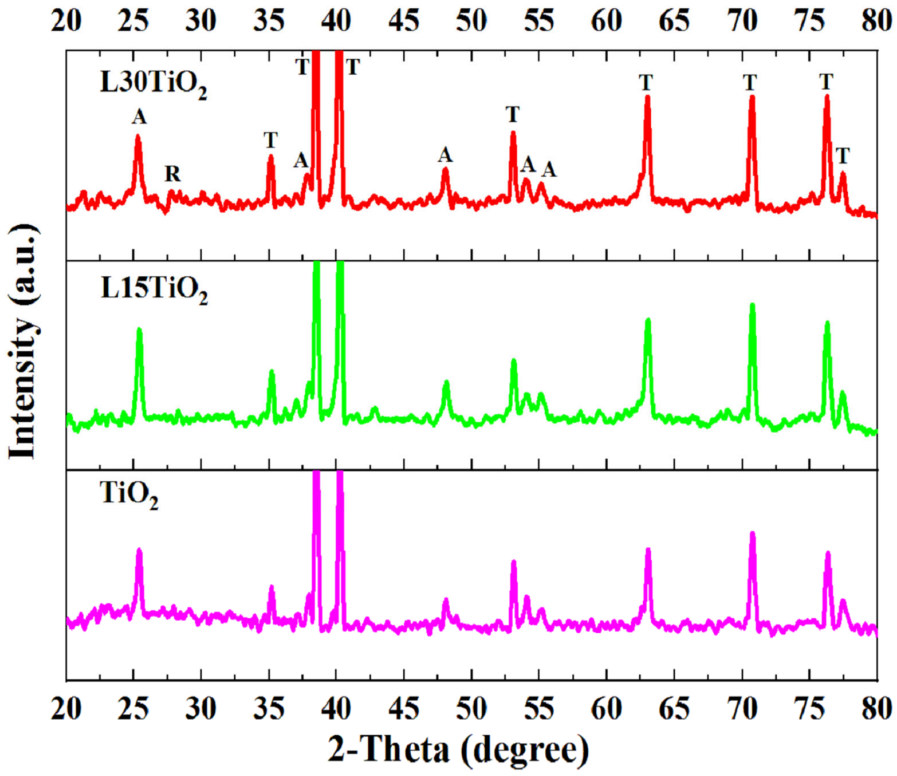

Figure 3. XRD patterns of TiO_2, $L15TiO_2$, and $L30TiO_2$.

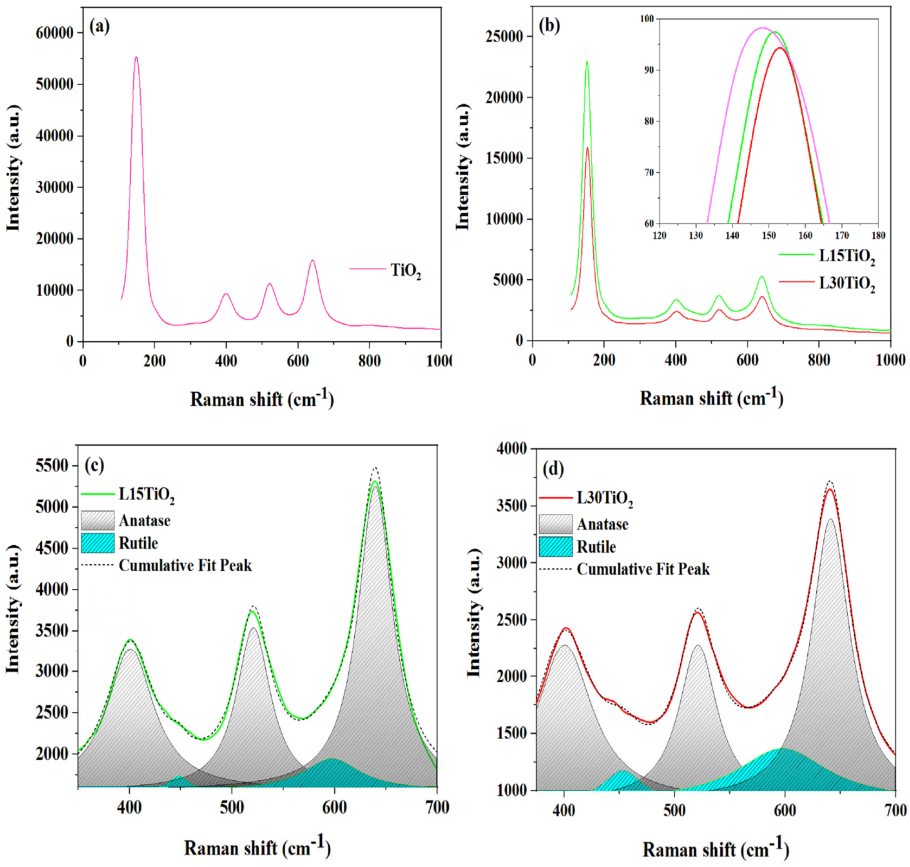

Figure 4. Raman spectra of (**a**) TiO_2, (**b**) $L15TiO_2$, and $L30TiO_2$, deconvolution of Raman spectra into the anatase and rutile phases for (**c**) $L15TiO_2$ and (**d**) $L30TiO_2$.

Upon applying and increasing the laser fluence from 15 to 30 J/cm^2, the relative intensity of the anatase signal decreases. The rutile fraction of L15TiO$_2$ and L30TiO$_2$ were obtained by fitting Lorentzian curves to the anatase and rutile-related Raman components in the 350–700 cm^{-1} range (Figure 4c,d). The deconvolution shows that the mixed Raman spectra of rutile and anatase in the region 300–780 cm^{-1} are composed of five active modes. The modes derived from the dominated anatase phase are centered around 400 cm^{-1} Bg$_{(1)}$, 520 cm^{-1} Ag$_{(1)}$, and 640 cm^{-1} Eg$_{(3)}$. Two active modes from the rutile phase were identified: Eg centered around 450 cm^{-1}, and Ag$_{(1)}$ centered around 605 cm^{-1} [41,42]. The coefficient of determination obtained in the final fit was $R^2 \geq 0.993$ and 0.997 for L15TiO$_2$ and L30TiO$_2$, respectively. These results are in accordance with previously obtained XRD analysis. Based on the Raman and XRD analyses, the non-laser-treated sample did not exhibit the presence of a rutile phase. However, the laser-treated samples exhibited the formation of a rutile phase. Therefore, it can be concluded that the calcination process, which was applied to all the samples at 450 °C, did not result in the formation of a rutile phase in the laser-treated samples. It is worth noting that the rutile phase starts to appear above 500 °C, and its quantity increases with a further increase in the annealing temperature [43,44]. It can be concluded that the formation of a rutile phase is a consequence of the laser irradiation treatment.

In order to determine the chemical valence state and surface components of the L30TiO$_2$ sample, which was chosen as a representative one based on photocatalytic measurements described later on, X-ray photoelectron spectroscopy (XPS) was used to detect its chemical composition and bonding configuration. During the fitting, the GL(30) function was used, and the intensity ratio between Ti 2p$_{3/2}$ and Ti 2p$_{1/2}$ was limited to 2:1. The survey spectrum of the L30TiO$_2$ sample is shown in Figure 5a. The Ti 2p spectrum (Figure 5b) showed distinct Ti 2p$_{3/2}$ and 2p$_{1/2}$ peaks at 458.8 and 464.5 eV, respectively, indicating the presence of Ti–O bonds in L30TiO$_2$. The 2p$_{3/2}$ and 2p$_{1/2}$ peaks at binding energies of 457.9 and 463.2 eV were assigned to Ti^{3+} [15,45]. The existence of Ti^{3+} species is attributed to the reduction of Ti^{4+}. The ratio of Ti^{4+}/Ti^{3+} phases is 68/32 at%, calculated by the peak area ratio. The primary peaks in the O 1s spectrum (Figure 5c) are attributed to the O lattice of TiO$_2$ (530.0 eV), -OH (532.5 eV) bonds, and the O-atoms in the vicinity of V_O (530.9 eV) [26,46]. Based on XPS spectrum analysis, the L30TiO$_2$ sample showed the formation of V_O/Ti^{3+}. These defects effectively prevented the recombination of photoinduced electron-hole pairs.

Heat treatment in a vacuum or the absence of oxidizing species causes O_2 to be lost, and Ti^{3+} is formed. Under usual thermal conditions, only about 1% of the atoms in the lattice can be reduced to Ti^{3+}. TiO$_2$ containing Ti^{3+} can be produced by various methods such as UV irradiation, laser, plasma-treating, inert-gas annealing, etc. [47,48]. Laser treatment can improve this phenomenon and achieve improved photocatalysis. Laser irradiation of a Ti substrate forms a heterojunction phase and oxygen vacancies/Ti^{3+} on the surface of the TiO$_2$ layer. Subsequently, electrochemical anodization results in various TiO$_2$ nanostructures that directly or indirectly contain heterojunctions and oxygen vacancies/Ti^{3+}.

3.3. Optical Properties

To study the optical properties of the obtained samples, reflection spectra were measured (Figure 6a), and Tauc's plot was prepared for the samples (Figure 6b). The calculation is based on the following Equation (2),

$$\alpha h\nu = A(h\nu - Eg)^n \quad (2)$$

where α was the absorption coefficient; hν was the Planck constant and light frequency; A was the proportionality; Eg was the band gap energy; n was the optical frequency [49]. The literature gives different values (ranging from 3.0 to 3.2 eV) to determine the optical bandgap of TiO$_2$, depending on the anatase/rutile phase. [43]. However, after analyzing Tauc's plot in Figure 6b, it can be observed that the gap values of TiO$_2$ do not change

significantly with increasing laser irradiance. The obtained values show a small difference but remain in a narrow range of about 3.2 eV for all TiO_2 samples. It is worth noting that there is a broad peak in the range of 500 to 700 nm in the laser-treated samples, which is caused by the light trapping effect that is probably the result of the obtained defect structures, as can be observed in the FESEM images [45].

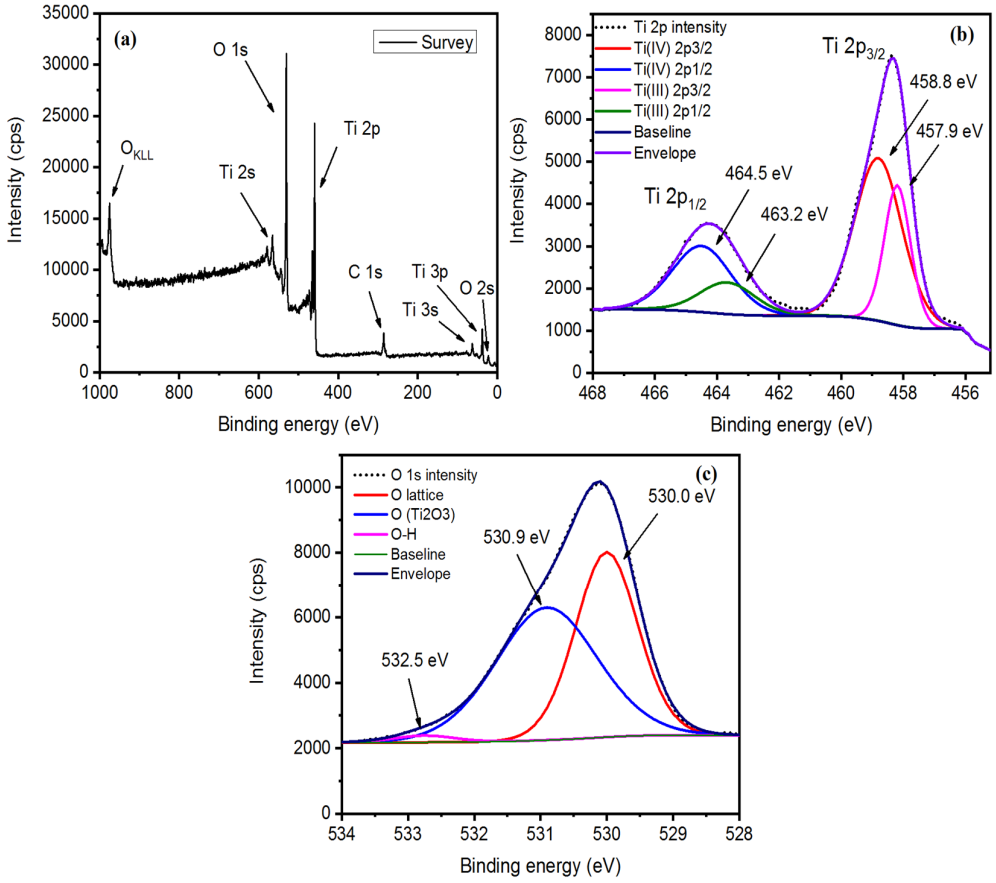

Figure 5. (**a**) The survey XPS spectrum, (**b**) Ti 2p and (**c**) O 1s XPS spectrum of $L30TiO_2$.

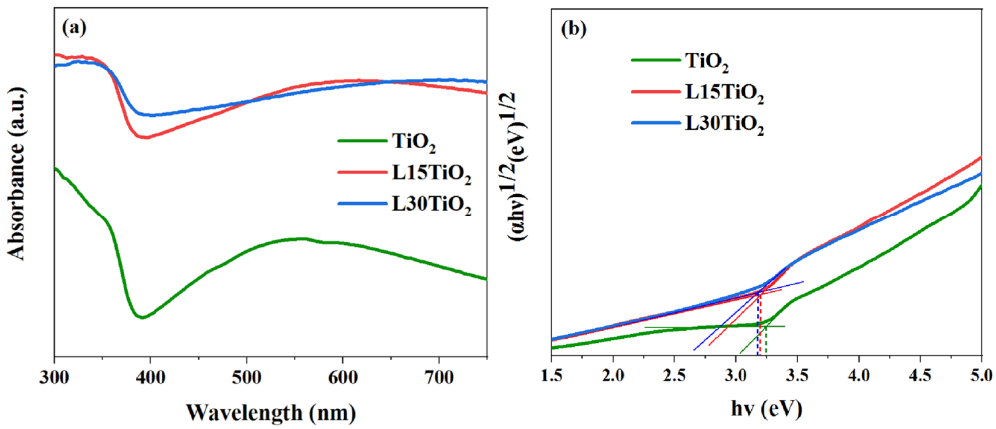

Figure 6. (**a**) UV–vis spectra of TiO_2, $L15TiO_2$, $L30TiO_2$, and (**b**) the transformed diffuse reflectance spectra.

The results above show that the photocatalytic activity of TiO_2 with phase junction, Ti^{3+}, and V_O is significantly improved. During photocatalytic reactions, electrons flow from rutile to anatase through the phase-junction, while holes move in the opposite direction, effectively separating photoexcited e^-/h^+ pairs [50,51]. By forming a sublevel potential beneath the TiO_2 conductive band, V_O and Ti^{3+} increase the rate of electron transfer

and reduce the recombination of e^-/h^+ pairs. Electrons travel from the valence band to the conduction band, which separates the photogenerated charge carriers, aiding in the development of catalytic processes [7,15].

3.4. Photocatalytic Properties

The photocatalytic properties of TiO_2, $L15TiO_2$, and $L30TiO_2$ were evaluated by testing their ability to degrade a certain concentration (4 mg/L) of CBF solution, which was used as a model organic pollutant. UV/Vis spectroscopy was used to monitor the photocatalytic degradation process of CBF, which was scanned between 200–350 nm and is shown in Figures 7a, S2 and S3, for $L30TiO_2$, $L15TiO_2$, TiO_2, respectively. Control experiments demonstrated that the concentration of CBF was unchanged in the absence of either irradiation or photocatalyst, implying that CBF was considerably stable and degradation by itself was negligible. The results are shown in Figure 7b, indicating that $L15TiO_2$ (71.4%) and $L30TiO_2$ (85.1%) exhibit better photocatalytic performance than TiO_2 (54.8%). The change in CBF concentration was followed by its characteristic absorption band (λ = 275 nm) (inset Figure 7a) [52].

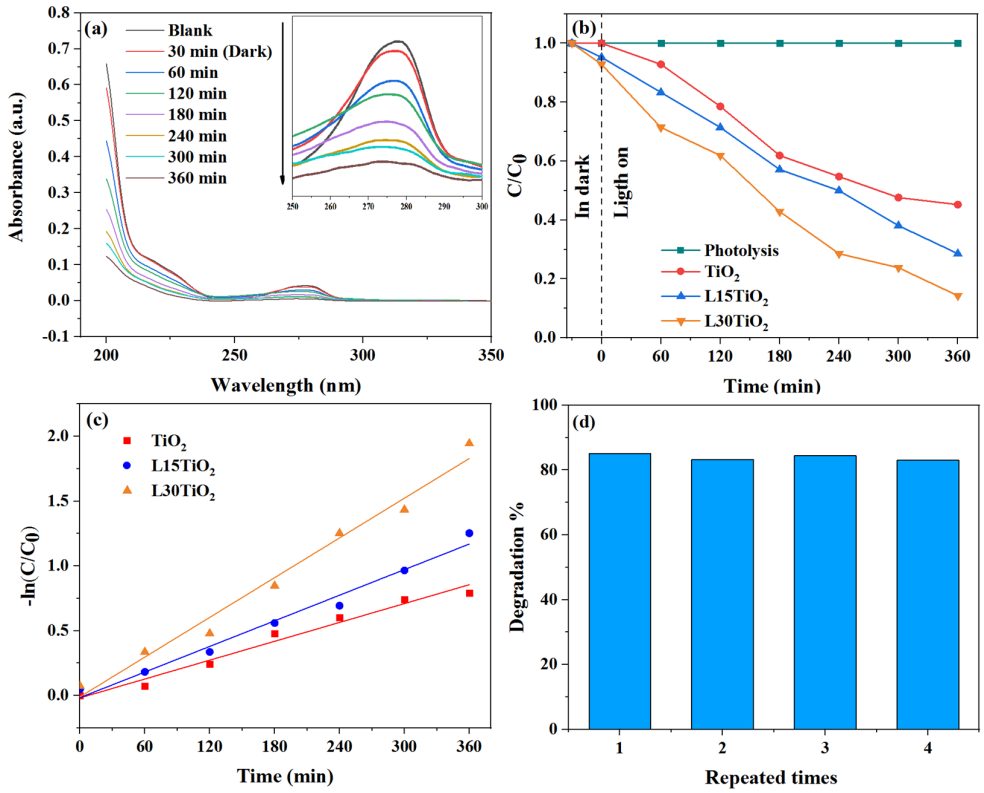

Figure 7. Photocatalytic degradation with $L30TiO_2$ measured with (**a**) UV-Vis, (**b**) rate of TiO_2, $L15TiO_2$, and $L30TiO_2$ for degradation of CBF under simulated sunlight irradiation, (**c**) kinetic fit of the degradation of CBF, (**d**) photocatalytic degradation of CBF with $L30TiO_2$ for four cycles.

The introduction of atomic-scale defects Ti^{3+} and V_O in the $L15TiO_2$ and $L30TiO_2$ samples was a crucial step that significantly reduced the recombination of e^- and h^+, thereby improving the photocatalytic activity of the irradiated samples. To better understand the rate of photocatalytic degradation of CBF with laser-irradiated TiO_2 photocatalysts, kinetic constants were calculated following the formula for pseudo-first-order kinetics (Equation (3)) [53]:

$$-ln\left(\frac{C}{C_0}\right) = k_1 t \quad (3)$$

where k_1 is the pseudo-first-order rate constant, and Co and C are the CBF concentrations at time t = 0 min and t = t min, respectively. The kinetic constants for the degradation of CBF with TiO_2, $L15TiO_2$, and $L30TiO_2$ are 0.0024 min^{-1}, 0.0033 min^{-1}, and 0.0051 min^{-1}, respectively (Figure 7c), and the linear regression correlation coefficients of the degradation experiment kinetic processes were 0.976, 0.982, and 0.981 for TiO_2, $L15TiO_2$, and $L30TiO_2$, respectively. The CBF degradation half-times can be determined from rate constants and are 289 min, 210 min, and 136 min for TiO_2, $L15TiO_2$, and $L30TiO_2$, respectively. Figure 7d shows the result of the recycling experiment performed for four cycles with an $L30TiO_2$, which is another important indicator for evaluating the photocatalytic performance of photocatalysts in terms of stability. After each cycle of photodegradation, $L30TiO_2$ was rinsed with water and dried. This result is compared with the available literature, and is listed in Table 1.

Table 1. Photocatalytic efficiencies of the TiO_2-based photocatalyst in different systems for carbofuran degradation.

Serial Numbers	Photocatalyst	Catalyst Concentration.	Light Source	CBF Concentration	Degradation/Time	References
1.	TiO_2	1.43 g/L	Sunlight	55 mg/L	100%/420 min	[54]
2.	GAC-TiO_2 + H_2O_2	5 mg/L	UV	50 mg/L	100%/68 min	[55]
3.	FeNT + PMS	0.5 g/L	Vis LED	0.015 mM	100%/7 min	[56]
4.	GAC-TiO_2	5 mg/L 5 mg/L	UV	50 mg/L 100 mg/L	100%/90 min 100%/120 min	[57]
5.	TiO_2	/	Sunlight	4 mg/L	85.1%/360 min	This study

V_O acts as an active site to adsorb oxygen from the air and convert it into superoxide radical anions by accepting electrons generated from excited semiconductors [58]. This enhances the degradation efficiency of organic pollutants. It could be concluded that laser ablation plays a key role in improving photocatalytic properties by forming V_O/Ti^{3+} in the laser-treated TiO_2 photocatalyst. The electrochemical formation of TiO_2 nanotube arrays on metallic titanium shows great potential in producing highly effective photocatalytic material for water purifiers. Therefore, micro and nanostructured TiO_2 on a Ti substrate has a large specific surface area, high light harvesting efficiency due to higher light scattering, high electron transport facilitated by the nanostructures, and good adhesion between TiO_2 and the titanium substrate [43]. The possibility of reusing TiO_2 in photocatalytic oxidation technology is enabled by its good adhesion to Ti substrate, which is not feasible when TiO_2 is used as a suspended powder [59].

3.5. Photocatalytic Degradation Products

The GC-MS technique was used to identify the main CBF products formed during the photocatalytic degradation in the presence of the $L30TiO_2$ sample. To extract the intermediates, 5 mL of irradiated CBF solution was withdrawn and then extracted with 1 mL of dichloromethane and shaken vigorously. The mixture was then analyzed with an Agilent GC 7890B/5977B mass detector. An HP-5 MS capillary column (30 m × 0.25 mm i.d., thickness of 0.25 µm) and helium as the carrier gas at a flow rate of 1.5 mL/min was used. The GC oven temperature was programmed as follows: initially held at 80 °C, increased to 210 °C at a rate of 10 °C/min and held for 3 min, then raised from 210 to 305 °C at a rate of 30 °C/min and finally held at 305 °C for 5 min. The injector and detector temperatures were maintained at 220 °C and 230 °C, respectively. The mass spectrometer was operated in the full-scan electron-impact (EI) mode at 70 eV [60]. From the MS spectrum confirmation presented in (Figure 8a), it has been established that the peak with a retention time of 11.95 min is carbofuran. Additionally, Figure 8b shows the MS spectrum of the peak at 6.71 min. Upon interpretation of the MS spectrum, this peak has been attributed to carbofuran phenol (2,3-dihydro-2,2-dimethylbenzofuran-7-ol). This product is the result of the cleavage of the carbamate group in carbofuran. Other degradation products may exist

in the photocatalytic system but may not have been detected due to their low concentration, extraction efficiency, and limited sensitivity in GC-MS.

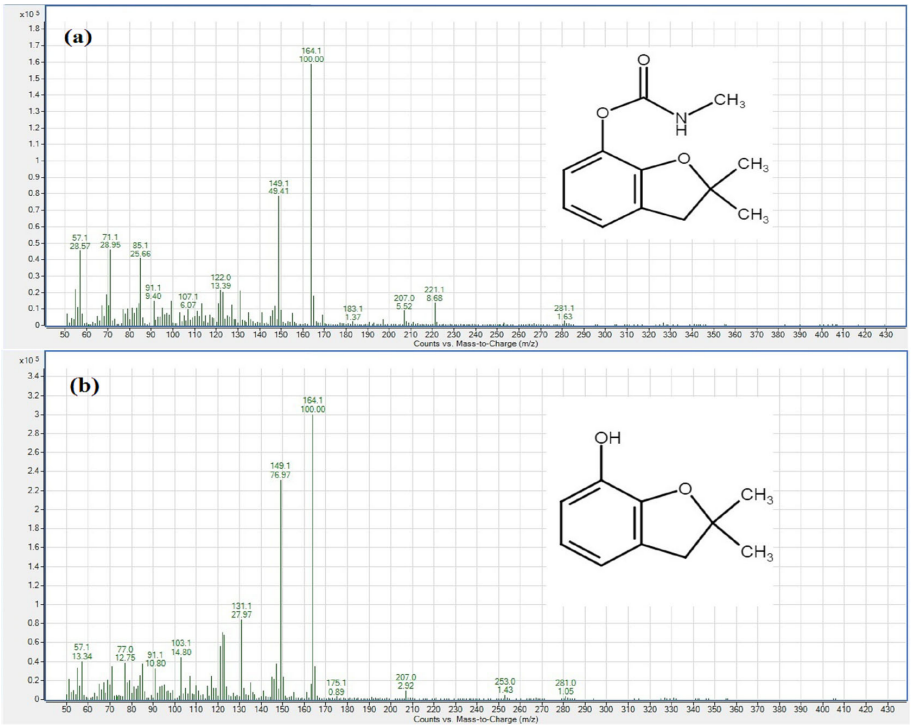

Figure 8. MS spectrum of (**a**) carbofuran and (**b**) carbofuran phenol.

The mechanism of photocatalytic degradation of carbofuran is shown in Figure 9. The first step in the photocatalytic degradation of carbofuran occurs when water undergoes a base hydrolysis reaction [61]. The carbamate group is separated from the molecule, and 2,3-dihydro-2,2-dimethylbenzofuran-7-ol and carbamic acid form. The C-O bond of the carbamate group is cleaved by a hydroxyl radical attack from carbofuran resulting in the formation of a phenolic anion and cation on the basic nitrogen. The phenolic anion can react with water by accepting a proton to form the intermediate 2,3-dihydro-2,2-dimethylbenzofuran-7-ol. Similarly, the cation can also react with water to abstract OH- to form the unstable carbamic acid and further degrades to methylamine and carbon dioxide [61]. It is expected that the furan and/or benzene rings will open, resulting in the formation of additional oxidative products [32,62].

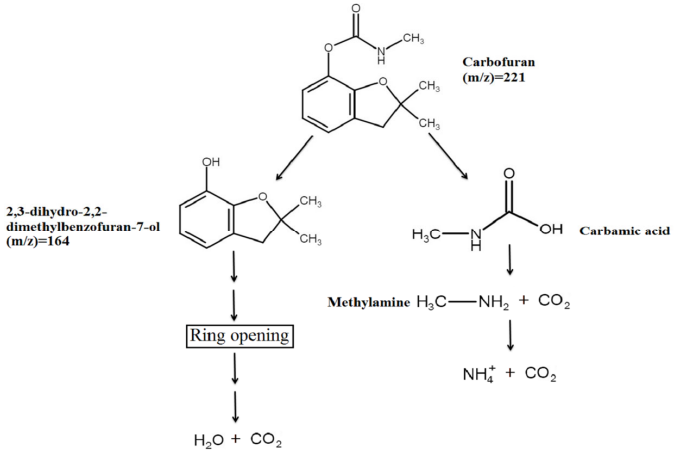

Figure 9. Proposed photocatalytical degradation pathway of carbofuran by L30TiO_2.

4. Conclusions

In summary, this study investigated the effect of using Nd:YAG picosecond pulsed laser irradiation at 1064 nm output with two different fluencies and with electrochemical anodization and their effect on the photocatalytic properties of TiO_2. The TiO_2 nanotube arrays were successfully manufactured by a two-step electrochemical anodization process on non-laser and laser-treated Ti meshes, followed by thermal annealing to ensure crystallization. FESEM results showed that the laser-treated TiO_2 samples have different morphologies of nanotube arrays that can be attributed to the Gaussian profile of the picosecond pulsed laser irradiation. Raman and XRD verified the presence of the anatase/rutile phase. The analysis of XPS spectra further confirms that Ti^{3+} species exist in laser-treated samples in the form of Vo/Ti^{3+} states. With the synergetic effects of phase junction and V_O/Ti^{3+}, the laser-treated TiO_2 samples showed a higher photodegradation rate (71.4%—L15TiO_2 and 85.1%—L30TiO_2) of CBF than non-laser-treated TiO_2 (54.8%), remaining stable and constant during four degradation cycles. This study shows that CBF undergoes photocatalytic degradation through a first-order reaction, initially producing 2,3-dihydro-2, 2-dimethylbenzofuran-7-ol, which then reacts to form other degradation products. Without laser treatment, the use of TiO_2 nanotube arrays resulted in a certain level of photocatalytic degradation of CBF. These results imply that this process can be improved by modifying the TiO_2 nanotube arrays by introducing V_O/Ti^{3+} into its structure by prior application of a picosecond pulsed laser irradiation.

Supplementary Materials: The following supporting information can be downloaded at https://www.mdpi.com/article/10.3390/photonics11030284/s1. Figure S1: The spectral distribution of the 300 W OSRAM Ultra-Vitalux lamp; Figure S2: Photocatalytic degradation with L15TiO_2 measured with UV-Vis; Figure S3: Photocatalytic degradation with TiO_2 measured with UV-Vis [63]. Reference [63] is included in the part.

Author Contributions: Conceptualization, M.T. and M.M.; formal analysis, M.T.; investigation, V.R., D.P. and. S.S.; writing—original draft preparation, M.T.; writing—review and editing, M.M. and N.K.; supervision, S.D.-B.; project administration, M.M.; funding acquisition, M.M. All authors have read and agreed to the published version of the manuscript.

Funding: The authors would like to thank the Ministry of Science, Technological Development and Innovation of the Republic of Serbia for the financial support to the research through institutional funding (Contract number: 451-03-66/2024-03/200017). N.K would like to thank the HrZZ-IP-2019-04-6418 project and the project Centre for Advanced Laser Techniques (CALT), co-funded by the European Union through the European Regional Development Fund under the Competitiveness and Cohesion Operational Programme (Grant No. KK.01.1.1.05.0001).

Institutional Review Board Statement: Not applicable.

Informed Consent Statement: Not applicable.

Data Availability Statement: Data are available upon reasonable request by the corresponding author.

Conflicts of Interest: The authors declare no conflict of interest.

References

1. Kapusta-Kołodziej, J.; Chudecka, A.; Sulka, G.D. 3D Nanoporous Titania Formed by Anodization as a Promising Photoelectrode Material. *J. Electroanal. Chem.* **2018**, *823*, 221–233. [CrossRef]
2. Ochiai, T.; Fujishima, A. Photoelectrochemical Properties of TiO_2 Photocatalyst and Its Applications for Environmental Purification. *J. Photochem. Photobiol. C Photochem. Rev.* **2012**, *13*, 247–262. [CrossRef]
3. Madkhali, N.; Prasad, C.; Malkappa, K.; Choi, H.Y.; Govinda, V.; Bahadur, I.; Abumousa, R. Recent Update on Photocatalytic Degradation of Pollutants in Waste Water Using TiO_2-Based Heterostructured Materials. *Results Eng.* **2023**, *17*, 100920. [CrossRef]
4. Ikreedeegh, R.R.; Hossen, A.; Tahir, M.; Aziz, A.A. A Comprehensive Review on Anodic TiO_2 Nanotube Arrays (TNTAs) and Their Composite Photocatalysts for Environmental and Energy Applications: Fundamentals, Recent Advances and Applications. *Coord. Chem. Rev.* **2024**, *499*, 215495. [CrossRef]
5. Chen, D.; Cheng, Y.; Zhou, N.; Chen, P.; Wang, Y.; Li, K.; Huo, S.; Cheng, P.; Peng, P.; Zhang, R.; et al. Photocatalytic Degradation of Organic Pollutants Using TiO_2-Based Photocatalysts: A Review. *J. Clean. Prod.* **2023**, *268*, 121725. [CrossRef]

6. Guo, Q.; Zhou, C.; Ma, Z.; Yang, X. Fundamentals of TiO_2 Photocatalysis: Concepts, Mechanisms, and Challenges. *Adv. Mater.* **2019**, *31*, 1901997. [CrossRef] [PubMed]
7. Arenas-Hernandez, A.; Zuñiga Islas, C.; Moreno, M.; Calleja Arriaga, W.; Mendoza-Cervantes, J.C.; Carlos, N.; Ascencio-Hurtado, C.R.; Heredia Jiménez, A. Study of Oxygen Vacancies in TiO_2 Nanostructures and Their Relationship with Photocatalytic Activity. *Appl. Sci.* **2022**, *12*, 3690. [CrossRef]
8. Vukoje, I.D.; Tomašević-Ilić, T.D.; Zarubica, A.R.; Dimitrijević, S.; Budimir, M.D.; Vranješ, M.R.; Šaponjić, Z.V.; Nedeljković, J.M. Silver Film on Nanocrystalline TiO_2 Support: Photocatalytic and Antimicrobial Ability. *Mater. Res. Bull.* **2014**, *60*, 824–829. [CrossRef]
9. Dong, H.; Zeng, G.; Tang, L.; Fan, C.; Zhang, C.; He, X.; He, Y. An Overview on Limitations of TiO_2-Based Particles for Photocatalytic Degradation of Organic Pollutants and the Corresponding Countermeasures. *Water Res.* **2015**, *79*, 128–146. [CrossRef]
10. Thind, S.S.; Paul, M.; Hayden, J.B.; Joshi, A.; Goodlett, D.; McIndoe, J.S. A Highly Efficient Photocatalytic System for Environmental Applications Based on TiO_2 Nanomaterials. *Ind. Chem. Mater.* **2023**, *1*, 431–442. [CrossRef]
11. Hanaor, D.A.H.; Sorrell, C.C. Review of the Anatase to Rutile Phase Transformation. *J. Mater. Sci.* **2011**, *46*, 855–874. [CrossRef]
12. Luttrell, T.; Halpegamage, S.; Tao, J.; Kramer, A.; Sutter, E.; Batzill, M. Why Is Anatase a Better Photocatalyst than Rutile?-Model Studies on Epitaxial TiO_2 Films. *Sci. Rep.* **2015**, *4*, 4043. [CrossRef]
13. Chahrour, K.M.; Yam, F.K.; Lim, H.S.; Abdalrheem, R. Synthesis of Anodic TiO_2 Nanotube Arrays Annealed at 700 °C for UV Photodetector. *J. Phys. Conf. Ser.* **2020**, *1535*, 012012. [CrossRef]
14. Yang, S.; Tang, W.; Ishikawa, Y.; Feng, Q. Synthesis of Titanium Dioxide with Oxygen Vacancy and Its Visible-Light Sensitive Photocatalytic Activity. *Mater. Res. Bull.* **2011**, *46*, 531–537. [CrossRef]
15. Ji, Z.; Wu, J.; Jia, T.; Peng, C.; Xiao, Y.; Liu, Z.; Liu, Q.; Fan, Y.; Han, J.; Hao, L. In-Situ Growth of TiO_2 Phase Junction Nanorods with Ti^{3+} and Oxygen Vacancies to Enhance Photocatalytic Activity. *Mater. Res. Bull.* **2021**, *140*, 111291. [CrossRef]
16. Setviń, M.; Aschauer, U.; Scheiber, P.; Li, Y.F.; Hou, W.; Schmid, M.; Selloni, A.; Diebold, U. Reaction of O_2 with Subsurface Oxygen Vacancies on TiO_2 Anatase (101). *Science* **2013**, *341*, 988–991. [CrossRef] [PubMed]
17. Zheng, J.; Liu, C.; Wang, Z.; Shi, Y.; Hou, Y.; Bi, J.; Wu, L. Improving Photocatalytic Degradation of Enrofloxacin over TiO_2 Nanosheets with Ti^{3+} Sites by Coordination Activation. *Appl. Catal. A Gen.* **2023**, *660*, 119217. [CrossRef]
18. Bazzanella, N.; Bajpai, O.P.; Fendrich, M.; Guella, G.; Miotello, A.; Orlandi, M. Ciprofloxacin Degradation with a Defective TiO_{2-x} Nanomaterial under Sunlight. *MRS Commun.* **2023**, *13*, 1252–1259. [CrossRef]
19. Sarkar, A.; Khan, G.G. The Formation and Detection Techniques of Oxygen Vacancies in Titanium Oxide-Based Nanostructures. *Nanoscale* **2019**, *11*, 3414–3444. [CrossRef]
20. Machreki, M.; Chouki, T.; Tyuliev, G.; Žigon, D.; Ohtani, B.; Loukanov, A.; Stefanov, P.; Emin, S. Defective TiO_2 Nanotube Arrays for Efficient Photoelectrochemical Degradation of Organic Pollutants. *ACS Omega* **2023**, *8*, 21605–21617. [CrossRef]
21. Białous, A.; Gazda, M.; Grochowska, K.; Atanasov, P.; Dikovska, A.; Nedyalkov, N.; Reszczyńska, J.; Zaleska-Medynska, A.; Śliwiński, G. Nanoporous TiO_2 Electrode Grown by Laser Ablation of Titanium in Air at Atmospheric Pressure and Room Temperature. *Thin Solid Films* **2016**, *601*, 41–44. [CrossRef]
22. Medvids, A.; Onufrijevs, P.; Kaupužs, J.; Eglitis, R.; Padgurskas, J.; Zunda, A.; Mimura, H.; Skadins, I.; Varnagiris, S. Anatase or Rutile TiO_2 Nanolayer Formation on Ti Substrates by Laser Radiation: Mechanical, Photocatalytic and Antibacterial Properties. *Opt. Laser Technol.* **2021**, *138*, 106898. [CrossRef]
23. Blažeka, D.; Radičić, R.; Maletić, D.; Živković, S.; Momčilović, M.; Krstulović, N. Enhancement of Methylene Blue Photodegradation Rate Using Laser Synthesized Ag-Doped ZnO Nanoparticles. *Nanomaterials* **2022**, *12*, 2677. [CrossRef] [PubMed]
24. Laketić, S.; Rakin, M.; Momčilović, M.; Ciganović, J.; Veljović; Cvijović-Alagić, I. Influence of Laser Irradiation Parameters on the Ultrafine-Grained Ti[Sbnd]45Nb Alloy Surface Characteristics. *Surf. Coatings Technol.* **2021**, *418*, 127255. [CrossRef]
25. Laketić, S.; Rakin, M.; Momčilović, M.; Ciganović, J.; Veljović, Đ.; Cvijović-Alagić, I. Surface Modifications of Biometallic Commercially Pure Ti and Ti-13Nb-13Zr Alloy by Picosecond Nd:YAG Laser. *Int. J. Miner. Metall. Mater.* **2021**, *28*, 285–295. [CrossRef]
26. Zhang, S.; Zhi, S.; Wang, H.; Guo, J.; Sun, W.; Zhang, L.; Jiang, Y.; Zhang, X.; Jiang, K.; Wu, D. Laser-Assisted Rapid Synthesis of Anatase/Rutile TiO_2 Heterojunction with Function-Specified Micro-Zones for the Effective Photo-Oxidation of Sulfamethoxazole. *Chem. Eng. J.* **2023**, *453*, 139702. [CrossRef]
27. Fathi-Hafshejani, P.; Johnson, H.; Ahmadi, Z.; Roach, M.; Shamsaei, N.; Mahjouri-Samani, M. Laser-Assisted Selective and Localized Surface Transformation of Titanium to Anatase, Rutile, and Mixed Phase Nanostructures. *J. Laser Appl.* **2021**, *33*, 012014. [CrossRef]
28. Scanlon, D.O.; Dunnill, C.W.; Buckeridge, J.; Shevlin, S.A.; Logsdail, A.J.; Woodley, S.M.; Catlow, C.R.A.; Powell, M.J.; Palgrave, R.G.; Parkin, I.P.; et al. Band Alignment of Rutile and Anatase TiO_2. *Nature* **2013**, *12*, 10–13. [CrossRef] [PubMed]
29. Luo, Z.; Poyraz, A.S.; Kuo, C.H.; Miao, R.; Meng, Y.; Chen, S.Y.; Jiang, T.; Wenos, C.; Suib, S.L. Crystalline Mixed Phase (Anatase/Rutile) Mesoporous Titanium Dioxides for Visible Light Photocatalytic Activity. *Chem. Mater.* **2015**, *27*, 6–17. [CrossRef]
30. Zhang, X.; Lin, Y.; He, D.; Zhang, J.; Fan, Z.; Xie, T. Interface Junction at Anatase/Rutile in Mixed-Phase TiO_2: Formation and Photo-Generated Charge Carriers Properties. *Chem. Phys. Lett.* **2011**, *504*, 71–75. [CrossRef]

31. Wawrzyniak, J.; Karczewski, J.; Kupracz, P.; Grochowska, K.; Załęski, K.; Pshyk, O.; Coy, E.; Bartmański, M.; Szkodo, M.; Siuzdak, K. Laser-Assisted Modification of Titanium Dioxide Nanotubes in a Tilted Mode as Surface Modification and Patterning Strategy. *Appl. Surf. Sci.* **2020**, *508*, 145143. [CrossRef]
32. Mahalakshmi, M.; Arabindoo, B.; Palanichamy, M.; Murugesan, V. Photocatalytic Degradation of Carbofuran Using Semiconductor Oxides. *J. Hazard. Mater.* **2007**, *143*, 240–245. [CrossRef] [PubMed]
33. Yang, H.; Zhou, S.; Liu, H.; Yan, W.; Yang, L.; Yi, B. Photocatalytic Degradation of Carbofuran in TiO_2 Aqueous Solution: Kinetics Using Design of Experiments and Mechanism by HPLC/MS/MS. *J. Environ. Sci.* **2013**, *25*, 1680–1686. [CrossRef] [PubMed]
34. Tomašević, A.; Mijin, D.; Marinković, A.; Radišić, M.; Prlainović, N.; Đurović-Pejčev, R.; Gašić, S. The Photocatalytic Degradation of Carbofuran and Furadan 35-ST: The Influence of Inert Ingredients. *Environ. Sci. Pollut. Res.* **2017**, *24*, 13808–13822. [CrossRef]
35. Mishra, S.; Zhang, W.; Lin, Z.; Pang, S.; Huang, Y.; Bhatt, P.; Chen, S. Carbofuran Toxicity and Its Microbial Degradation in Contaminated Environments. *Chemosphere* **2020**, *259*, 127419. [CrossRef] [PubMed]
36. Luís, A.M.; Neves, M.C.; Mendonça, M.H.; Monteiro, O.C. Influence of Calcination Parameters on the TiO_2 Photocatalytic Properties. *Mater. Chem. Phys.* **2011**, *125*, 20–25. [CrossRef]
37. Thangavel, P.; Karuppanan, S.; Muthusamy Poomalai, P.; Sakthivel, A.; Nandagopalan, G.; Bellucci, S. Effect of Chelating Agents on the Structural, Optical, and Dye-Degradation Properties of Tungsten Oxide Nanoparticles. *Photonics* **2022**, *9*, 849. [CrossRef]
38. Rung, S.; Barth, J.; Hellmann, R. Characterization of Laser Beam Shaping Optics Based on Their Ablation Geometry of Thin Films. *Micromachines* **2014**, *5*, 943–953. [CrossRef]
39. Hill, M.; Wagenaars, E. Modelling of Plasma Temperatures and Densities in Laser Ablation Plumes of Different Metals. *Photonics* **2022**, *9*, 937. [CrossRef]
40. Haryński, Ł.; Grochowska, K.; Karczewski, J.; Ryl, J.; Siuzdak, K. Scalable Route toward Superior Photoresponse of UV-Laser-Treated TiO_2 Nanotubes. *ACS Appl. Mater. Interfaces* **2020**, *12*, 3225–3235. [CrossRef]
41. Zanatta, A.R. A Fast-Reliable Methodology to Estimate the Concentration of Rutile or Anatase Phases of TiO_2. *AIP Adv.* **2017**, *7*, 075201. [CrossRef]
42. An, X.; Hu, C.; Liu, H.; Qu, J. Hierarchical Nanotubular Anatase/Rutile/TiO_2(B) Heterophase Junction with Oxygen Vacancies for Enhanced Photocatalytic H_2 Production. *Langmuir* **2018**, *34*, 1883–1889. [CrossRef] [PubMed]
43. Roy, P.; Berger, S.; Schmuki, P. TiO_2 Nanotubes: Synthesis and Applications. *Angew. Chem.-Int. Ed.* **2011**, *50*, 2904–2939. [CrossRef] [PubMed]
44. Chen, X.; Mao, S.S. Titanium Dioxide Nanomaterials: Synthesis, Properties, Modifications and Applications. *Chem. Rev.* **2007**, *107*, 2891–2959. [CrossRef] [PubMed]
45. Liang, M.; Li, X.; Jiang, L.; Ran, P.; Wang, H.; Chen, X.; Xu, C.; Tian, M.; Wang, S.; Zhang, J.; et al. Femtosecond Laser Mediated Fabrication of Micro/Nanostructured TiO_{2-x} Photoelectrodes: Hierarchical Nanotubes Array with Oxygen Vacancies and Their Photocatalysis Properties. *Appl. Catal. B Environ.* **2020**, *277*, 119231. [CrossRef]
46. Kuang, J.; Xing, Z.; Yin, J.; Li, Z.; Tan, S.; Li, M.; Jiang, J.; Zhu, Q.; Zhou, W. Ti^{3+} Self-Doped Rutile/Anatase/TiO_2(B) Mixed-Crystal Tri-Phase Heterojunctions as Effective Visible-Light-Driven Photocatalysts. *Arab. J. Chem.* **2020**, *13*, 2568–2578. [CrossRef]
47. Kowalski, D.; Kim, D.; Schmuki, P. TiO_2 Nanotubes, Nanochannels and Mesosponge: Self-Organized Formation and Applications. *Nano Today* **2013**, *8*, 235–264. [CrossRef]
48. Xiong, L.B.; Li, J.L.; Yang, B.; Yu, Y. Ti^{3+} in the Surface of Titanium Dioxide: Generation, Properties and Photocatalytic Application. *J. Nanomater.* **2012**, *2012*, 9. [CrossRef]
49. Chahrour, K.M.; Yam, F.K.; Samuel, J.J.; Abdalrheem, R.; Beh, K.P.; Lim, H.S. Controlled Synthesis of Vertically Aligned Honeycomb TiO_2 Nanotube Arrays: Effect of High-Temperature Annealing on Physical Properties. *Appl. Phys. A Mater. Sci. Process.* **2019**, *125*, 440. [CrossRef]
50. Wang, W.K.; Chen, J.J.; Zhang, X.; Huang, Y.X.; Li, W.W.; Yu, H.Q. Self-Induced Synthesis of Phase-Junction TiO_2 with a Tailored Rutile to Anatase Ratio below Phase Transition Temperature. *Sci. Rep.* **2016**, *6*, 20491. [CrossRef] [PubMed]
51. Ullattil, S.G.; Abdel-Wahab, A. Self-Oxygenated Anatase-Rutile Phase Junction: Ensuring the Availability of Sufficient Surface Charges for Photocatalysis. *New J. Chem.* **2020**, *44*, 5513–5518. [CrossRef]
52. Atwan, A.A.; Elmehasseb, I.M.; Talha, N.; El-Kemary, M. Parameters Affecting Carbofuran Photocatalytic Degradation in Water Using ZnO Nanoparticles. *J. Chin. Chem. Soc.* **2020**, *67*, 1833–1842. [CrossRef]
53. Kovačević, M.; Živković, S.; Ognjanović, M.; Momčilović, M.; Relić, D.; Vasić Anićijević, D. In Silico Guided Design of Metal/Semiconductor Photocatalysts: A Case of Cu-Modified TiO_2 for Ciprofloxacin Degradation. *Materials* **2023**, *16*, 5708. [CrossRef] [PubMed]
54. Lopez-Alvarez, B.; Torres-Palma, R.A.; Peñuela, G. Solar Photocatalitycal Treatment of Carbofuran at Lab and Pilot Scale: Effect of Classical Parameters, Evaluation of the Toxicity and Analysis of Organic by-Products. *J. Hazard. Mater.* **2011**, *191*, 196–203. [CrossRef] [PubMed]
55. Vishnuganth, M.A.; Remya, N.; Kumar, M.; Selvaraju, N. Carbofuran Removal in Continuous-Photocatalytic Reactor: Reactor Optimization, Rate-Constant Determination and Carbofuran Degradation Pathway Analysis. *J. Environ. Sci. Heal.-Part B Pestic. Food Contam. Agric. Wastes* **2017**, *52*, 353–360. [CrossRef] [PubMed]
56. Abdelhaleem, A.; Chu, W. Insights into Peroxymonosulfate Activation for Carbofuran Degradation under Visible LED via a Double-Component Photocatalyst of Fe (III) Impregnated N-Doped TiO_2. *Chemosphere* **2019**, *237*, 124487. [CrossRef] [PubMed]

57. Vishnuganth, M.A.; Remya, N.; Kumar, M.; Selvaraju, N. Photocatalytic Degradation of Carbofuran by TiO_2-Coated Activated Carbon: Model for Kinetic, Electrical Energy per Order and Economic Analysis. *J. Environ. Manag.* **2016**, *181*, 201–207. [CrossRef] [PubMed]
58. Li, J.; Cheng, D.; Chen, Z.; Yang, L.; Zheng, L.; Wei, Z.; Ma, T.; Zhang, J.; Luo, Y. Oxygen Vacancy/Ti^{3+} Engineered TiO_2 Nanotube Arrays Prepared by in-Situ Exfoliation with H_2 Bubbles: A Visible-Light-Driven Self-Supporting Photocatalyst for Detoxfication of Chloraphenicol. *J. Environ. Chem. Eng.* **2021**, *9*, 106670. [CrossRef]
59. Huang, T.; Lu, J.; Xiao, R.; Wu, Q.; Yang, W. Enhanced Photocatalytic Properties of Hierarchical Three-Dimensional TiO_2 Grown on Femtosecond Laser Structured Titanium Substrate. *Appl. Surf. Sci.* **2017**, *403*, 584–589. [CrossRef]
60. Ma, Y.S.; Kumar, M.; Lin, J.G. Degradation of Carbofuran-Contaminated Water by the Fenton Process. *J. Environ. Sci. Health Part A* **2009**, *44*, 914–920. [CrossRef]
61. Bachman, J.; Patterson, H.H. Photodecomposition of the Carbamate Pesticide Carbofuran: Kinetics and the Influence of Dissolved Organic Matter. *Environ. Sci. Technol.* **1999**, *33*, 874–881. [CrossRef]
62. Katsumata, H.; Matsuba, K.; Kaneco, S.; Suzuki, T.; Ohta, K.; Yobiko, Y. Degradation of Carbofuran in Aqueous Solution by Fe(III) Aquacomplexes as Effective Photocatalysts. *J. Photochem. Photobiol. A Chem.* **2005**, *170*, 239–245. [CrossRef]
63. Ines, M.; Paolo, P.; Roberto, F.; Mohamed, S. Experimental Studies on the Effect of Using Phase Change Material in a Salinity-Gradient Solar Pond under a Solar Simulator. *Sol. Energy* **2019**, *186*, 335–346. [CrossRef]